Journal of Structural Geology, Vol. 11, No. 3, pp. 317 to 328, 1989
Printed in Great Britain

0191-8141/89 $03.00 + 0.00

Modelling of bed contours and cross-sections adjacent to planar normal faults

J. R. GIBSON, J. J. WALSH and J. WATTERSON

Department of Earth Sciences, University of Liverpool, P.O. Box 147, Liverpool L69 3BX, U.K.

(*Received* 18 *January* 1988; *accepted in revised form* 16 *August* 1988)

Abstract—The geometry of beds in the volume surrounding a single blind planar fault depends on: (i) the axial ratio of the fault surface ellipse, (ii) the ratio between the maximum displacement and the maximum dimension of the fault surface, (iii) the displacement distribution on the fault surface from the point of maximum displacement to zero displacement at the tip-line loop (fault surface displacement profile) and (iv) the rate at which the displacement decreases to zero along a normal to the fault surface (reverse drag displacement profile). These relationships, which are either known or can be estimated, are incorporated in a computer model which generates structural contours on horizons intersected by a planar fault. Structural contour patterns also vary with the pre-faulting dip and strike of beds, the dip and strike of the fault and the level at which a bed intersects the fault surface. When the boundary conditions are relaxed to include synsedimentary faults, the ratio of hangingwall to footwall displacement varies systematically with fault dip.

A synthetic structural contour map is matched with that of an actual fault. Model isopachs, based on simple depositional models, are generated for synsedimentary units. Cross-sections are generated for synsedimentary faults by sequential fault growth and sedimentary deposition, and show features similar to actual cross-sections. The soft-domino model is applicable primarily to dip-slip tectonic faults with maximum displacements of up to about 5 km; listric faults are not considered.

INTRODUCTION

DISPLACEMENTS in the rock volume containing a dip-slip fault vary along strike and down-dip, and also in the direction normal to the fault surface, but fault geometry is usually described and discussed in terms of two-dimensional cross-sections normal to the fault strike. The variation in displacement normal to the fault surface as expressed by reverse drag, or rollover, geometry has received more attention than the displacement variation parallel to fault surfaces. As sections normal to the fault strike allow assessment of the effects of changes in fault dip, many analyses concentrate on the mechanical and geometrical effects of changes in fault dip at the expense of other variables. Many faults imaged on seismic sections and measured in mines have more or less constant dips and we model here the displacement geometry in the volume containing a planar tectonic fault. Results are expressed either by synthetic contours on an horizon intersected by a fault or by cross-sections derived from the contours. In the soft-domino model fault displacement is accommodated by penetrative strains within the fault volume, which increase incrementally as the elastic strain accommodating each slip event is relaxed to permanent strain prior to the next event. The model is applicable to tectonic faults with maximum displacements up to 5 km, but some features of the model can be applied to larger faults. We do not consider gravity-driven faults with passive footwalls like those of landslips. The computer model is directly applicable only to planar normal or reverse faults, but could be modified for oblique-slip or strike-slip displacements.

The soft-domino model is an alternative to current methods of quantitative analysis of reverse drag profiles, which incorporate two questionable assumptions. The first assumption is that hangingwall rollover is necessarily a result of listric fault plane geometry (Verrall 1981, Wernicke & Burchfiel 1982, Gibbs 1983, 1984a, Davison 1986, White *et al.* 1986); that is, the vertical displacement component decreases with increasing distance from a shallowing fault with constant displacement along its surface. It is thereby implied that displacement of beds due to a fault of constant dip does not decrease with distance from the fault and therefore persists indefinitely. This assumption is also implicit in recent modifications of the Chevron model which allows displacement to vary along the fault surface (Wheeler 1987, Williams & Vann 1987). We maintain that displacement decreases with distance from all tectonic faults, as is shown by geodetic measurements on neotectonic faults. The second questionable assumption is that the footwalls of all normal faults are passive, apart from minor isostatic uplift (Gibbs 1983, 1984a, Barr 1985). This assumption is not credible in the case of blind faults, for which the symmetrical displacements on either side of strike-slip faults provide a good model. On neotectonic normal or reverse faults that intersect the surface and are not driven by gravity, footwall reverse drag does occur, as would be expected of structures which grow as elastic dislocations (Savage & Hastie 1966, Stein & Barrientos 1985). A further purpose of the model is, therefore, to generate synthetic contours which can be used to examine structural and stratigraphic development in the footwalls of synsedimentary faults.

Displacement is used throughout to refer to displacement accumulated during the active life of a fault. Slip is used to refer to movement in a single seismic event or seismic cycle. Displacement at the fault surface, of one

side relative to the other, is either D (maximum displacement at the centre of a fault) or d (displacement elsewhere on the fault surface). The displacement along the fault surface of either hangingwall or footwall relative to a fixed datum is either D (maximum) or d (less than maximum). Displacement of a point within the volume surrounding a fault, but not at the fault surface, is d^1 and always refers to displacement relative to a fixed datum. References to slip in a single event follow the same convention, i.e. U, u, U, u and u^1.

FACTORS CONTROLLING DISPLACEMENT GEOMETRY

Displacements in the volume containing a single blind planar fault are determined by the following fixed relationships which characterize an ideal fault (Barnett *et al.* 1987): (i) the ratio of the maximum displacement to the maximum dimension of the fault surface, (ii) the displacement distribution on the fault surface from the point of maximum displacement to zero displacement at the tip-line loop (the fault surface displacement profile), (iii) the rate at which displacement (d^1) decreases to zero along a normal to the fault surface (the reverse drag displacement profile) and (iv) the distribution of displacement between footwall and hangingwall. These relationships are all known to within limits acceptable for modelling simple ideal faults. Bed geometry is also affected by the following variables (i) the axial ratio of the fault surface ellipse, (ii) the fault dip, (iii) the pre-faulting dip of beds and their strike relative to that of the fault and (iv) the level at which a bed intersects the fault surface. We assume that all displacements are parallel to one another and to the fault surface and, by computing the displacements at all points in the volume containing a model fault, derive structural contours of horizons intersected by the fault. We derive structural contours of an horizon at any stage of fault growth and, when the boundary conditions are relaxed to include faults which intersect the surface (synsedimentary faults), calculate the variation in pre-compaction bed thicknesses in the vicinity of the fault.

Elliptical fault surfaces

Surfaces of single blind normal faults are approximately elliptical. Fault surface ellipses have horizontal major axes and axial ratios of 1.25–3.0 (Rippon 1985, Barnett *et al.* 1987, Walsh & Watterson 1989). Synthetic contours illustrated here were generated for a fault surface axial ratio of 2, but any value can be input to the modelling program.

Width–displacement ratio

The width of a fault is defined as the maximum dimension of the fault surface in a direction normal to the slip direction. For normal faults the width is therefore the long axis of the fault surface ellipse. No confusion in terms arises so long as the map length of a fault is recognized as being the length of the fault trace. The ratio of maximum dimension (W) to maximum displacement (D) on measured fault surfaces varies by two orders of magnitude (from 5 to 500). In principle, W/D can vary over 7 orders of magnitude from the value characteristic of single slip events on active faults ($ca\ 3 \times 10^{-5}$) to values on ancient faults. The ratio decreases with the size of fault, and

$$D = cW^2, \tag{1}$$

where c is a function of material properties (Walsh & Watterson 1988a). The most important material property is shear modulus (G), and

$$D \propto W^2/G^2. \tag{2}$$

The model input is either D or W together with either G or W/D.

Fault surface displacement profile

A normalized curve of displacement (d) vs distance from fault centre (r) is referred to as the fault surface displacement profile. Using the characteristic slip profile for single slip events along faults and a fault growth model described by Watterson (1986), Walsh & Watterson (1987) derived the following expression for the steady state fault surface displacement profile on multiple slip event faults

$$d_n = 2(((1 + r_n)/2)^2 - r_n^2)^{1/2}(1 - r_n), \tag{3}$$

where d_n is the normalized displacement (d/D) at a point on a radius of the fault ellipse and r_n is the normalized radial distance (r) from the fault centre ($r_n = r/R$, where R is the fault radius).

Standard reverse drag profile

This is a normalized curve describing the change in displacement along a normal to a fault surface. Normalized displacement (d_n^1) and normalized distance (r_n^1) are given by $d_n^1 = d^1/d$ and $r_n^1 = r^1/R^1$, where r^1 = distance from fault surface and R^1 = reverse drag radius.

As faults rarely form normal to horizons, reverse drag profiles of horizons will not be identical with the standard profile. An empirical expression for the steady state profile of multiple event faults is (Barnett *et al.* 1987)

$$(1 - y)^2 + (1 - x)^2 = 1, \tag{4}$$

where y = normalized displacement and x= normalized distance from a fault. A more accurate empirical description of the standard reverse drag profile is derived below.

Geodetically measured reverse drag profiles for single slip events on several strike-slip faults are given by Kasahara (1981). A theoretical curve fitted to data for the Imperial Valley (1940) earthquake (see Fig. 1a), shows slip (U) to be 2 m at the fault and u^1 effectively zero at 40 km from the fault. Taking 40 km as the maximum reverse drag radius (R) the ratio $U/2R = 5 \times 10^{-5}$, similar to the ratio, slip (U)/length of fault trace

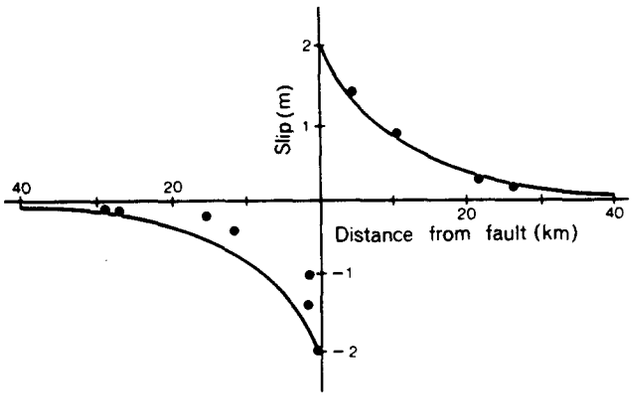

a

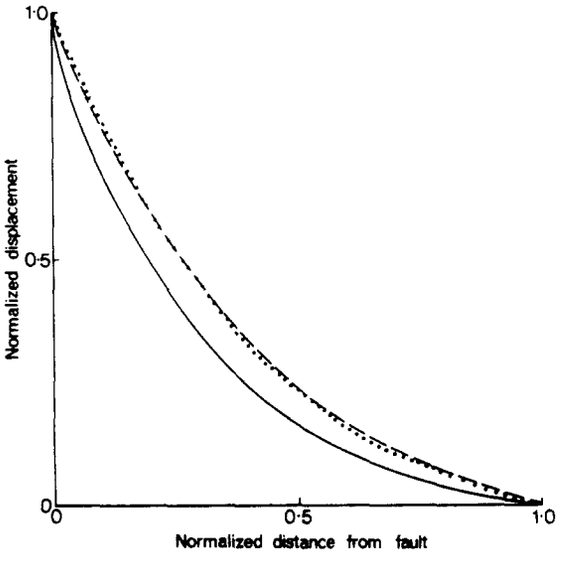

b

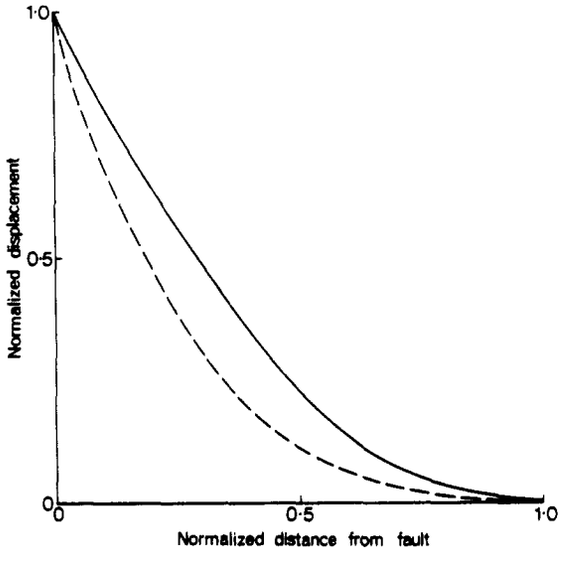

c

Fig. 1. (a) Geodetic data (solid circles) for Imperial Valley (1940) earthquake strike-slip displacements (u^1) and best-fit elastic dislocation profile (solid line). Redrawn from Kasahara (1981, fig. 4.9). (b) Normalized reverse drag profiles for single-slip events on strike-slip faults. Solid line—Imperial Valley (1940) earthquake (Kasahara 1981), dotted line—Tango (1927) earthquake (Chinnery & Petrak 1968), broken line—Idu (1930) earthquake (Chinnery & Petrak 1968). (c) Normalized reverse drag profiles for the hangingwall (solid line) and footwall (broken line) vertical displacements associated with the Borah Peak (1983) earthquake (Stein & Barrientos 1985).

typical for single slip events (Scholz *et al.* 1986). An empirical expression for the normalized reverse drag profile of the Imperial Valley (1940) earthquake is

$$y = e^{-3.5x} - 0.03x, \quad (5)$$

where y is the normalized slip ($u_n^1 = u^1/U$) and x is the normalized distance (r_n^1) in a fault-normal direction (Fig. 1b). Figures 1(b) & (c) show normalized reverse drag profiles for the Tango (1927) and Idu (1930) strike-slip earthquake events (Chinnery & Petrak 1968) and the Borah Peak (1983) normal dip-slip event (Stein & Barrientos 1985). For the Tango (1927) and Idu (1930) events (Fig. 1b), R is taken as half the length of the surface traces assumed by Chinnery & Petrak (1968). However, at these distances the displacements are not zero but are 19 and 11%, respectively, of the slip (U) at the fault surface, so R is underestimated. Data for the Borah Peak (1983) earthquake event do not represent a standard reverse drag profile for a single slip event, because the fault surface is inclined at about 45° to the displaced surface measured (Fig. 1c; Stein & Barrientos 1985).

If R equals half the length of the surface trace, the elastically deformed volume surrounding a blind circular fault is spherical (Barnett *et al.* 1987), an approximation which observation and theory show to be valid (Savage & Hastie 1966, Mansinha & Smylie 1971). If this approximation holds, R for single events is linearly related to the slip (U) and will increase as the fault grows. The steady state standard reverse drag profile can then be calculated in exactly the same way as the fault surface displacement profile (Walsh & Watterson 1987). The derived empirical expression is

$$y = e^{-5.5x} - 0.004x, \quad (6)$$

where x is the normalized distance (r_n^1) and y is the normalized displacement, d_n^1 (Fig. 2).

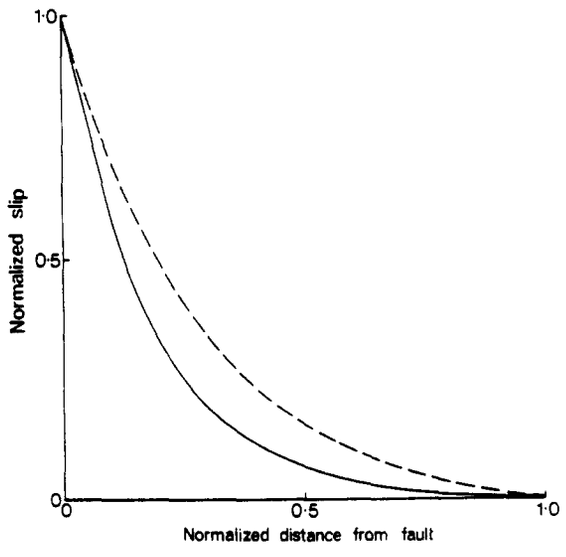

Fig. 2. Standard normalized reverse drag profiles for single-slip events (broken line) and multiple event steady state (solid line), from equations (5) and (6).

Disadvantages of errors inherent in using data for a single earthquake event are outweighed by the advantage of using real data. Any expression derived by elastic theory needs modification to limit the potentially very large, or infinite, reverse drag radii to practical values. The differences between results obtained by different methods and approximations for the single event profile have, in practice, little effect on the general form of the derived steady state profile for multiple events. Uncertainty regarding the tightness of the profile may lead to slight inaccuracy in the spacing of model structural contours.

If R is the standard reverse drag radius at the point of maximum displacement (D) then the average drag radius, R^1, at a point on the fault surface at which the displacement is d, is taken as:

$$R^1 = R(d/D)^{1/2}. \quad (7)$$

We assume for modelling purposes that R on an elliptical fault is the mean of the major and minor radii of the ellipse, so that the limit of reverse drag is an ellipsoidal surface with the fault surface a principal plane of the ellipsoid.

Hangingwall/footwall displacement ratio

For blind faults, displacement is taken to be distributed equally between footwall and hangingwall, that is, the same symmetry as shown by strike-slip faults. Barnett *et al.* (1987) recognized that an assumption of equal D for footwall uplift and hangingwall subsidence is probably invalid for synsedimentary faults. This conclusion is confirmed by geodetic data for single slip events which demonstrate a systematic difference between hangingwall subsidence and footwall uplift associated with dip-slip faults (Fig. 3, Savage & Hastie 1966, Jackson & McKenzie 1983, Stein & Barrientos 1985). By analogy with elastic dislocations adjacent to a free surface (Steketee 1958a, b), vertical faults should show footwall uplift equal to hangingwall subsidence, whereas non-vertical faults should show an asymmetry that increases with decreasing fault dip (Fig. 4a, Savage &

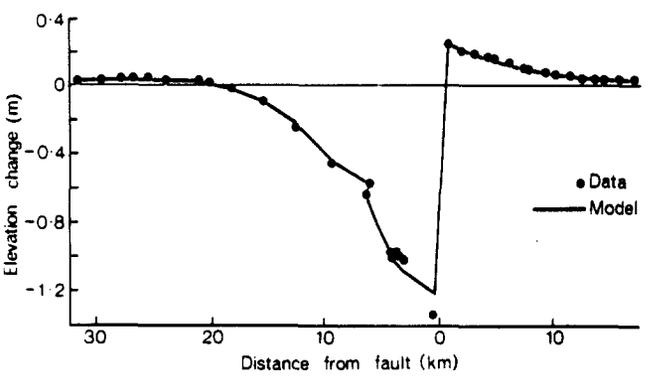

Fig. 3. Geodetic data (solid circles) showing vertical displacements associated with the Borah Peak (1983) event on the Lost River Fault, Idaho. The normal dip-slip component of displacement is 2.15 m and the fault dip is 45 ± 5° from surface to 13 ± 3 km depth. The solid line is the coseismic planar fault elastic dislocation model curve. Redrawn from Stein & Barrientos (1985, fig. 4).

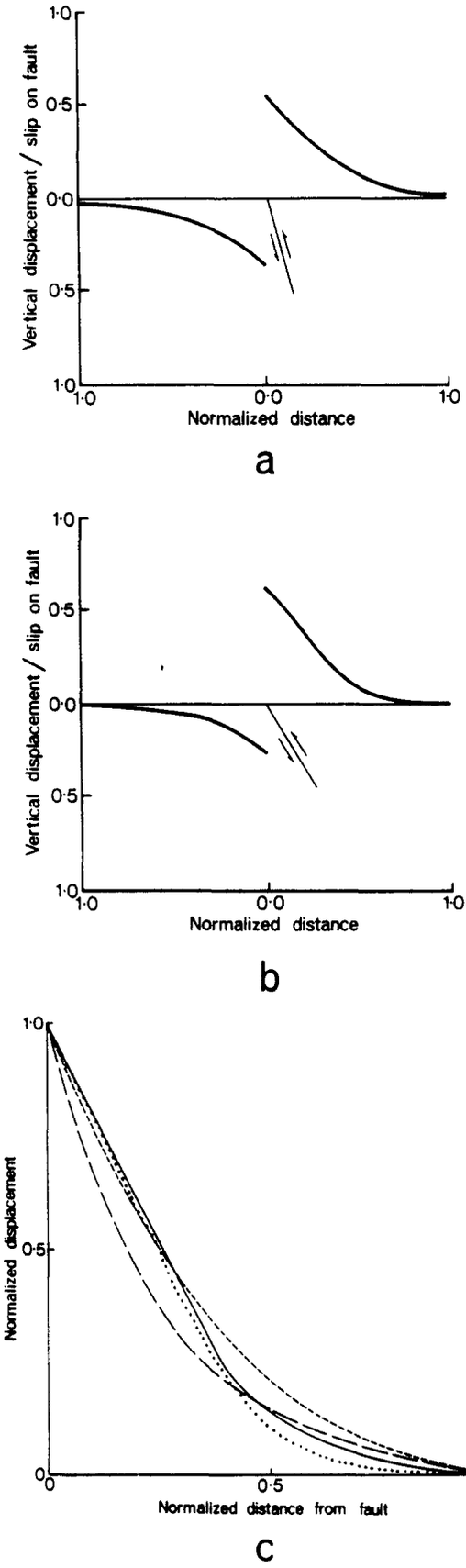

Fig. 4. (a) and (b) Cross-sections, based on an elastic dislocation model, showing the distribution of vertical displacement between hangingwalls and footwalls for single-slip events on reverse faults with dips of 60° (a) and 75° (b) (modified from Savage & Hastie 1966, and Mansinha & Smylie 1971). (c) Normalized reverse drag profiles for the fault events shown in (a) and (b): 75° dipping dip-slip reverse fault, hangingwall—solid line, footwall—long dashed line (from Mansinha & Smylie 1971); 60° dipping dip-slip normal fault, hangingwall—dotted line, footwall—short dashed line (from Savage & Hastie 1966).

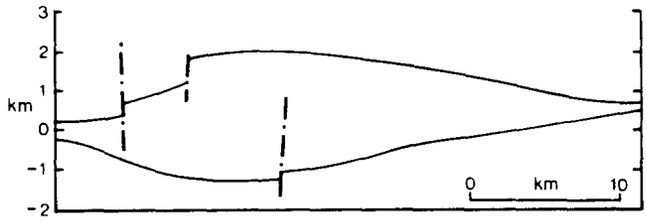

Fig. 5. Horizon–separation diagram showing the footwall and hangingwall cutoffs of the Tiim phonolite unit on the Saimo Fault, Kenya Rift. Cutoff separation represents the vertical component of displacement. Redrawn from Chapman *et al.* (1978, fig. 6).

Hastie 1966, Mansinha & Smylie 1971). The asymmetry is such that uplift is reduced relative to subsidence on normal faults and conversely on reverse faults (Savage & Hastie 1966, Mansinha & Smylie 1971); the asymmetry can be thought of in terms of the volume difference between the elastic deformation fields on either side of a dipping fault intersecting the free surface. From the results given by Savage & Hastie (1966) and Mansinha & Smylie (1971), the percentage contribution of hangingwall displacement (HW) to the total displacement, on normal faults steeper than 30°, is approximately

$$HW = 110 - 2\theta/3, \quad (8)$$

where θ = fault dip (in degrees). For single slip events on a fault intersecting the free surface, the reverse drag profiles are different in hangingwall and footwall (Fig. 4b), but the difference is relatively small and has not been incorporated in the model.

Horizon–separation diagrams can be used to estimate the ratio of footwall/hangingwall displacement on faults, as is shown in Fig. 5 for the Saimo Fault in the Kenya Rift system (Chapman *et al.* 1978). The separation of a pre-faulting horizon has a footwall/hangingwall displacement ratio of *ca* 45:55. The dip of the fault is not given but the fault set of which it is a part has a mean dip of 63°. The geometry of footwall and hangingwall cut-off lines on horizon–separation diagrams also reflects the fault surface displacement profile; the displacement (d) profiles of cut-off lines shown in Fig. 5 are similar to those predicted by the model (Walsh & Watterson 1989).

SYNTHETIC CONTOUR PATTERNS AND CROSS-SECTIONS

Method of construction

Contour maps and cross-sections are constructed by calculating the displacements at the nodes of a square grid or along a line. For each point on the chosen horizon, a perpendicular is dropped to the fault surface and the displacement (d) at that point on the fault surface is calculated using equation (3). The displacement (d^1) at the appropriate point on the horizon is determined using equations (6) and (7). Correction is made for footwall/hangingwall asymmetry, equation (8).

Blind faults

The basic pattern. Figure 6(a) shows calculated structural contours and a cross-section for a simple case in which the fault dips at 60° and the horizon is horizontal prior to faulting; the contoured horizon intersects the fault at its centre (i.e. the point of maximum displacement). As several relationships interact to produce this contour pattern, some confidence is engendered by the general similarity to real contour patterns (see Barnett *et al.* 1987, figs. 9–11).

Width/displacement ratio. Variation in W/D affects structural contours mainly in respect of the contour spacing, i.e. the dips of the contoured horizon, with similar patterns maintained for a wide range of W/D values. Heave/width ratio changes with W/D producing systematic variations on the general pattern. All the synthetic contours illustrated are for W/D = 20, corresponding to that expected for a fault of 1 km maximum displacement in hard sandstone (Walsh & Watterson 1988a). Contour values, and elevations on cross-sections, for smaller faults with W/D = 20, can be obtained by linear scaling of elevation changes with the chosen maximum displacement.

The effects of changes in fault size are shown in Fig. 6(f). As dip changes for smaller faults are slight and imperceptible on true scale sections (Fig. 6f), the synthetic contour patterns and cross-sections presented are for large faults, which have low W/D values. Figure 6(f) shows why, especially in the case of small faults, the displacement geometry is often best represented by a contour map.

Effects of varying level of fault/horizon intersection. Contours on initially horizontal horizons intersected by the same fault but at different levels, are shown in Figs. 6(a), (c) and (d). Figure 6(c) is for an horizon intersecting above the centre of the fault, at a distance of 0.66 × the minor radius of the fault surface ellipse (radial distance = 0.66); Fig. 6(d) is for an horizon intersecting the fault at 0.33 radial distance below the centre. The difference in symmetry between the two patterns is due to the non-vertical fault dip and occurs even when displacement is distributed equally between footwall and hangingwall (Barnett *et al.* 1987). Changes in horizon dip are quite small (Figs. 6c & d), even for a large fault, unless the horizon intersects near to the fault centre.

Variation of fault dip. The effect of variation in fault dip is seen by comparing Figs. 6(a) and 7(f). Decrease in fault dip is accompanied by a decrease in the vertical component of displacement and, for given fault dimensions, changes in the reverse drag profiles. For example, with the 45° dipping fault shown in Fig. 7(f), horizon dips close to the fault are less steep than with a similar 60° dipping fault (Fig. 6a).

Variation of initial horizon dip. The greatest variation

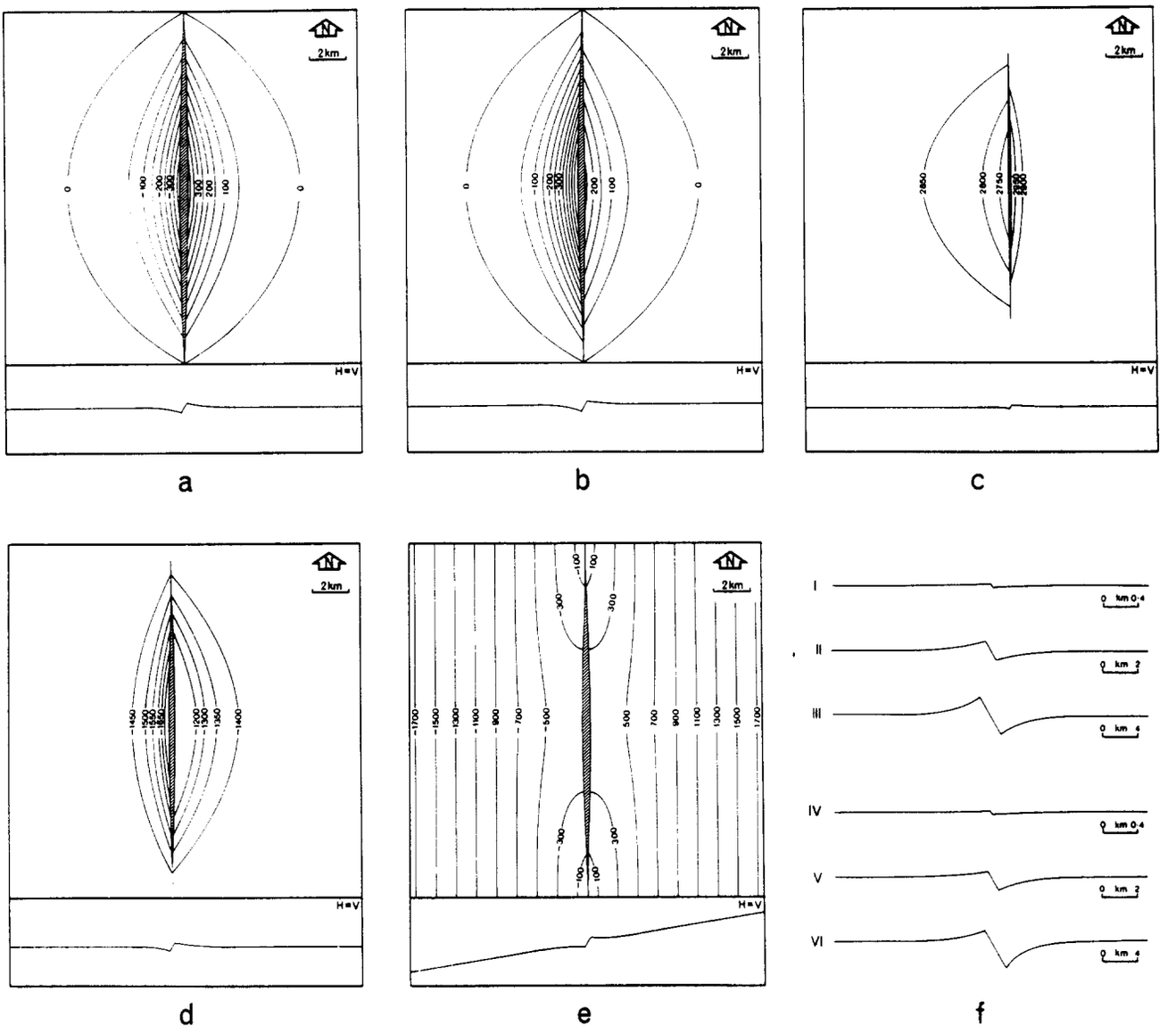

Fig. 6. (a)–(e) Synthetic contours and cross-sections for an horizon intersected by a blind normal fault (a, c, d, e) or synsedimentary fault (b). Fault parameters: maximum displacement—1 km, fault width—20 km, down-dip radius—5 km, rollover radius—7.5 km. Contours in metres with zero datum at either fault centre (blind faults) or pre-faulting free surface (synsedimentary fault). Fault dip 60° W in each case. (a) Initially horizontal horizon intersecting centre of blind fault. (b) As (a) but synsedimentary fault. (c) As (a) but horizon intersects minor axis of fault ellipse at radial distance of 0.66 above centre of the fault. (d) As (a) but horizon intersects fault ellipse at radial distance of 0.33 below centre of the fault. (e) As (a) but with initial horizon dip 10° W. (f) True-scale cross-sections of synthetic reverse drag profiles for 60° dipping blind faults (i, ii, iii) and synsedimentary faults (iv, v, vi) of different sizes. Hangingwall/footwall displacement ratio is 70:30 for synsedimentary faults. Faults (i) and (iv): maximum displacement—50 m, W/D ratio—100. Faults (ii) and (v): maximum displacement—1.2 km, W/D ratio—20. Faults (iii) and (vi): maximum displacement—5 km, W/D ratio—10. W/D ratios are those expected in hard sandstone with shear modulus of *ca* 10 GPa. Note changes in angles of intersection between horizon and fault.

in contour patterns is due to variations in the initial amount and direction of horizon dip relative to the direction of the fault dip. The effect is seen by comparing Figs. 6(e) and 7(a), (b), (c) & (e); the fault displacements and dimensions are the same in all cases.

Faults intersecting a free surface

Figures 6(b) and 7(d) show contour patterns and cross-sections for two synsedimentary faults. We assume, for modelling purposes, that the maximum displacement (D) on the faults is at the stratigraphic level of the free surface at the time of fault initiation. The contours are those on this surface and it is assumed that neither erosion nor deposition takes place during fault growth. Although unrealistic, this assumption is useful for considering displacements of the initial free surface. Displacement distribution between footwall and hangingwall is as expressed in equation (8).

The extent to which the assumption of no erosion or deposition is geologically unrealistic can be quantified by considering the time likely for accumulation of 1 km displacement. An estimated 1414 seismic cycles are required to grow a fault with a maximum displacement of 1 km (Watterson 1986). The recurrence time for intraplate earthquakes is thousands of years, with 10,000

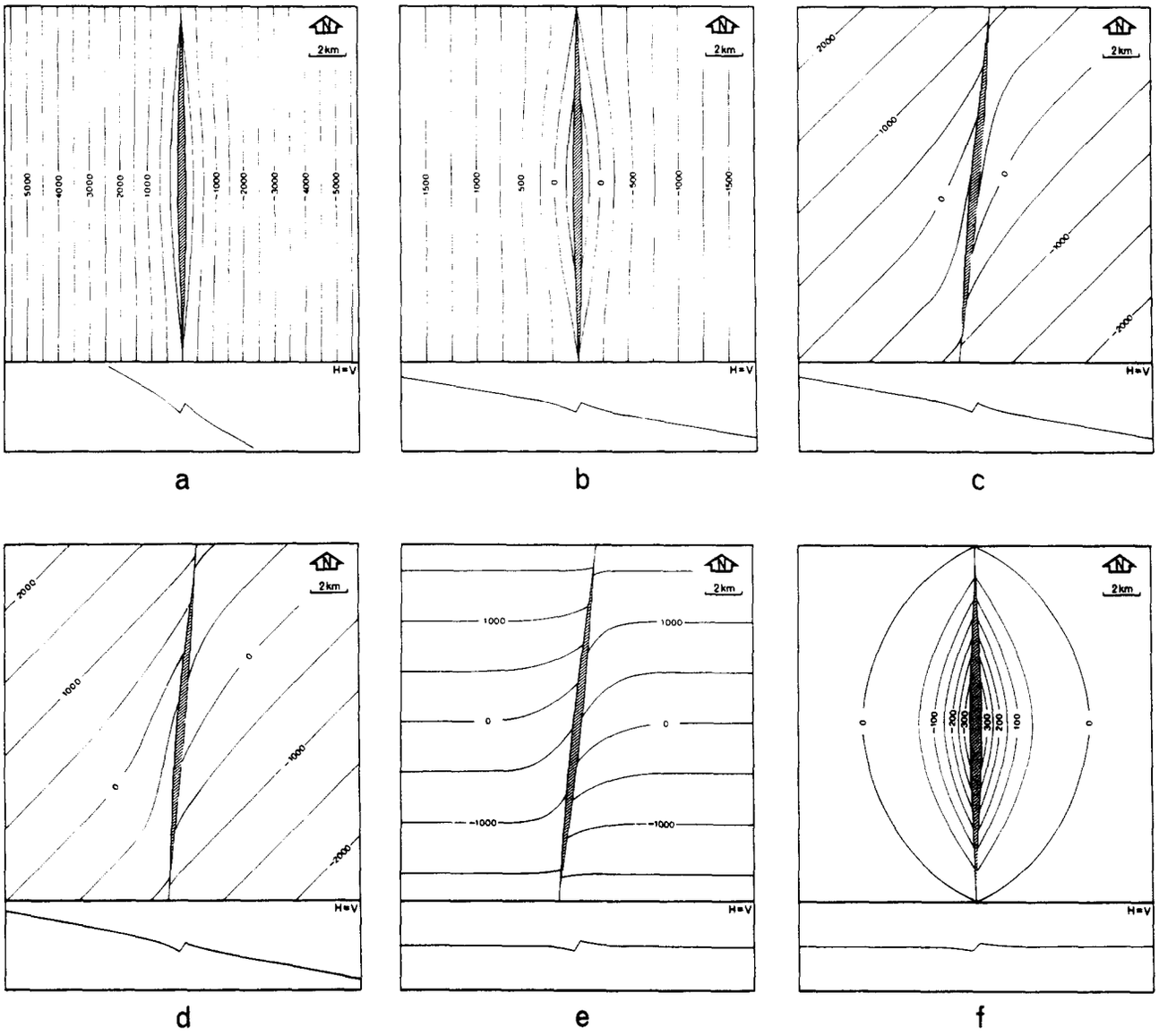

Fig. 7. Synthetic contours and cross-sections for an horizon intersected by a blind normal fault (a, b, c, e, f) or a synsedimentary fault (d). Fault parameters and zero contour datum as for Fig. 6. Fault dips 60° W in all cases except (f). (a) Initial horizon dip 30° E with horizon intersecting centre of fault. (b) As (a) but horizon dip 10° E. (c) As (a) but horizon dip 10° to 135°. (d) As (c) but synsedimentary fault. (e) As (a) but horizon dip 10° to 180°. (f) Fault dip 45° W and horizon initially horizontal.

years a representative value (Scholz *et al.* 1986). These values suggest that it takes 14.14×10^6 years to accummulate 1 km displacement, allowing ample time for surficial processes to be effective.

APPLICATIONS

Several features which may be associated with real faults are not incorporated in the model. Changes of fault dip with depth and with formation lithology are likely with many types of fault and both regular and irregular dip changes will affect the displacement geometry. Curved fault traces are common and are necessary consequences of lateral changes in fault dip (Walsh & Watterson 1988b). Displacement gradients on faults may differ from those modelled if disconnected segments of the same fault overlap (Walsh & Watterson 1989), as at fault jogs (Sibson 1986). No account is taken of normal drag which can have a marked effect on structural contours close to faults (Barnett *et al.* 1987). Isostatic footwall uplift is not incorporated in the model but is unlikely to be significant when footfall uplift is synchronous with each slip event. Current isostatic models for footwall uplift are based on instantaneous fault displacement and are two-dimensional (Kusznir *et al.* 1988).

For modelling purposes we assume that all reverse drag displacement is accommodated by a continuous deformation, whereas on many faults a significant proportion is accommodated on antithetic faults. An obvious shortcoming of the current model is that only single isolated faults are considered and such faults are not usual: in most real cases the displacement fields of adjacent faults overlap and structural contours are resultants of displacements on two or more faults.

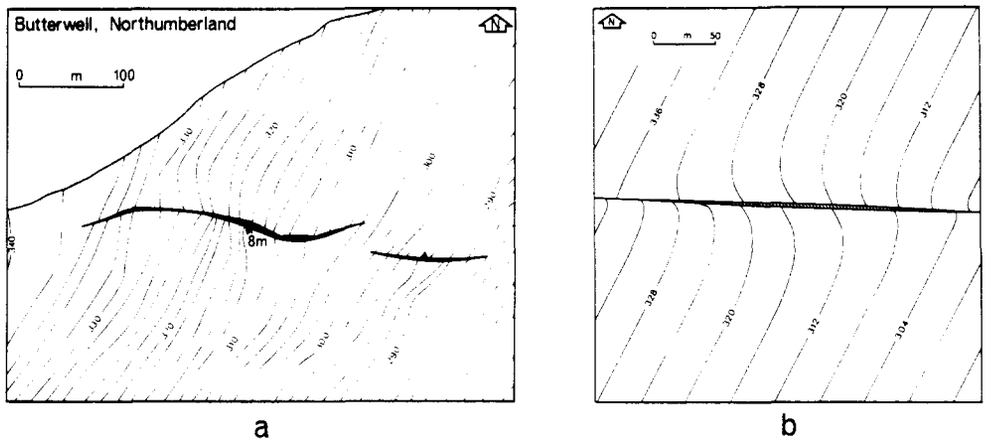

Fig. 8. (a) Structural contours on excavated coal seam, Butterwell Opencast Site, Northumberland. Contours in metres above O.D. Deflection and changes of spacing of contours close to the 8 m throw fault are due primarily to hangingwall and footwall reverse drag. (b) Synthetic contour pattern matching the essential features of the contours in (a). Model fault parameters: width 275 m, displacement 9.13 m, dip 68° to 180°, down-dip radius 500 m, reverse drag radius 750 m, horizon dip 7° to 298°.

Given these shortcomings the principal use of the current model is in demonstrating the influence of each of the variables, so that contour patterns can be correctly interpreted. A further use of the model is derivation of contour patterns matching those associated with actual faults and so deriving the fault parameters. Backward modelling is currently possible only for very simple cases such as that shown in Figs. 8(a) & (b). The main differences between the real and modelled contours are due to the non-planar nature of the actual fault. Figure 9(a) is a cross-section of a synsedimentary fault in the northern North Sea, which shows both footwall and hangingwall reverse drag and a footwall/hangingwall displacement ratio of 20:80. This ratio indicates an original fault dip of 45°, which, allowing for compaction, is consistent with the present fault dip of *ca* 35°. Normalized reverse drag profiles for this fault are broadly consistent with the theoretical profiles (Fig. 9b).

A further application of the model is in examining stratigraphic relationships and formation thicknesses adjacent to synsedimentary faults. The structural contours represent idealised model isopachs of syn-faulting formations (Fig. 6b). In the case of the footwall sediments the contours represent the inverse of the isopachs (Fig. 6b).

Isopachs adjacent to synsedimentary faults can be derived by plotting surface contours for successive stages of fault growth and by taking compactional effects into account. Figure 10 shows synthetic cross-sections derived for two simple cases of syn-faulting sedimentation, in which the sedimentation rate is proportional to the rate of fault displacement. Each of the five stratigraphic units shown is equivalent in time to a 200 m displacement on a fault with a total displacement of 1 km. In Figs. 10(a) & (b), the sediment surface is maintained at the level of the footwall cutoff, whereas in Fig. 10(c) only the hangingwall subsidence is infilled. The post-basement sequence has been compacted by 30%, corresponding to a final depth of burial of about 3 km.

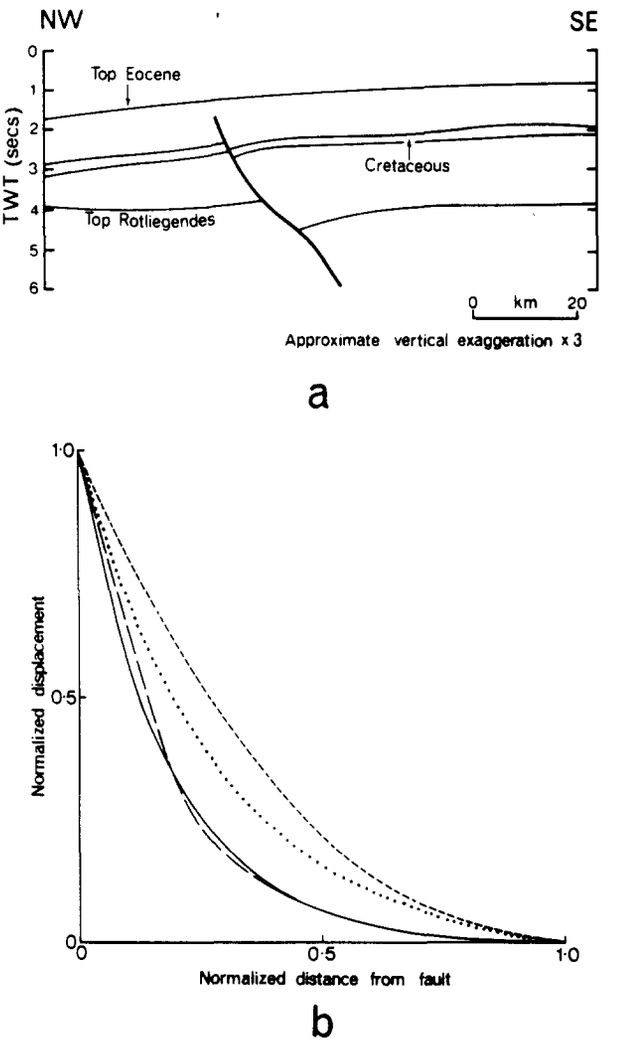

Fig. 9. (a) Cross-section from the Western margin of the Norwegian Platform adjacent to the Central Graben showing faulting of Top Rotliegendes, after Beach (1985, fig. 1b). (b) Normalized reverse drag profiles at Top Rotliegendes for hangingwall (short dash) and footwall (long dash) of fault shown in (a). The standard single event (dotted) and the multiple event steady state profiles, from Fig. 2, are shown for comparison.

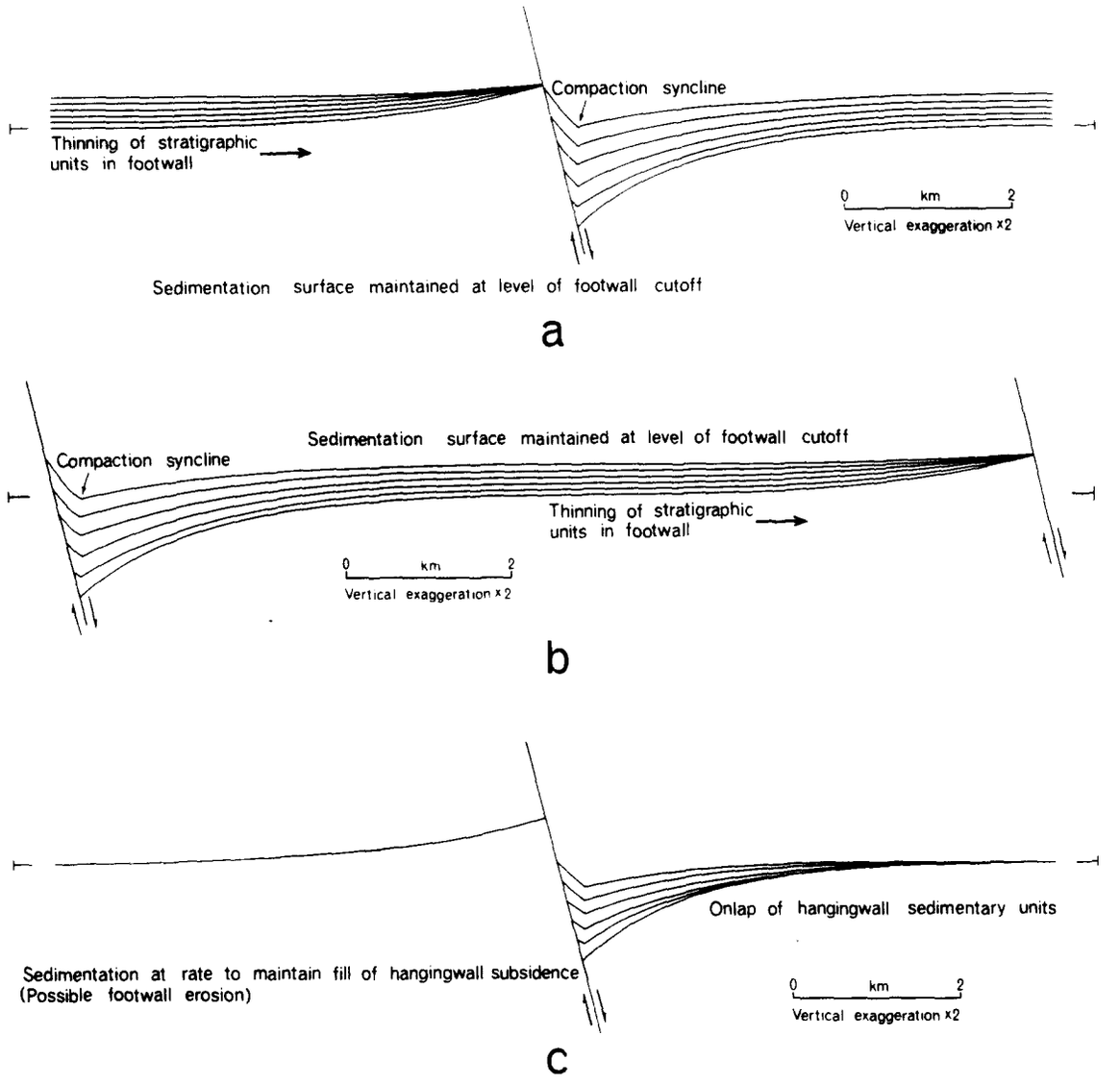

Fig. 10. Synthetic cross-sections of synsedimentary faults (see text for details). Model sedimentation rates are proportional to the fault displacement rate with the level of sedimentary fill maintained at the footwall cutoff in (a) and restricted to the hangingwall subsidence trough in (c). (b) Sediment thickness variation and bedding inflection expected between two faults of the type shown in (a). Fault displacements 1 km, widths 20 km, reverse drag radii 7.5 km, compaction of sediments 30%.

producing compactional synclines within the hangingwalls.

For each stratigraphic unit to be made equivalent to 200 m fault displacement is unrealistic, because the time interval represented by each of the units is then different (Watterson 1986). On a 1 km fault the displacements accumulated after each of five equal time intervals would be 40, 160, 360, 641 and 1000 m, i.e. the final 500 m of displacement would occur in less than 25% of the time during which the fault was active. A condition that sedimentation rate be proportional to fault displacement rate would require progressively higher sedimentation rates as a fault grows. The later stages of fault growth are therefore those in which a fault scarp is more likely to develop and, if emergent, be subjected to erosion. Footwall uplift is more difficult to recognize when erosion of an emergent footwall has taken place. Hangingwall stratigraphy of the synthetic cross-section (Fig. 10c) is similar to that predicted by listric fault models, but footwall uplift, apart from minor isostatic effects, is not a feature of listric faulting (Jackson & McKenzie 1983). Onlap of the hangingwall sequence onto the pre-faulting basement is an essential part of the model and is seen in many hangingwall sequences (Fig. 11c, see also Enfield & Coward 1987); onlap is not an essential feature of listric fault models because the rollover radius is assumed to be constant throughout the growth of the fault. The effects of two faults of the same size separated by a distance of twice the reverse drag radius are shown in Fig. 10(b).

The synthetic cross-sections and the model footwall stratigraphy shown in Fig. 10 bear comparison with cross-sections of faults from a variety of depositional situations (Figs. 11 and 12), and reproduce some of the characteristics of the footwall reservoirs. A section from the North Viking Graben is shown for comparison (Fig.

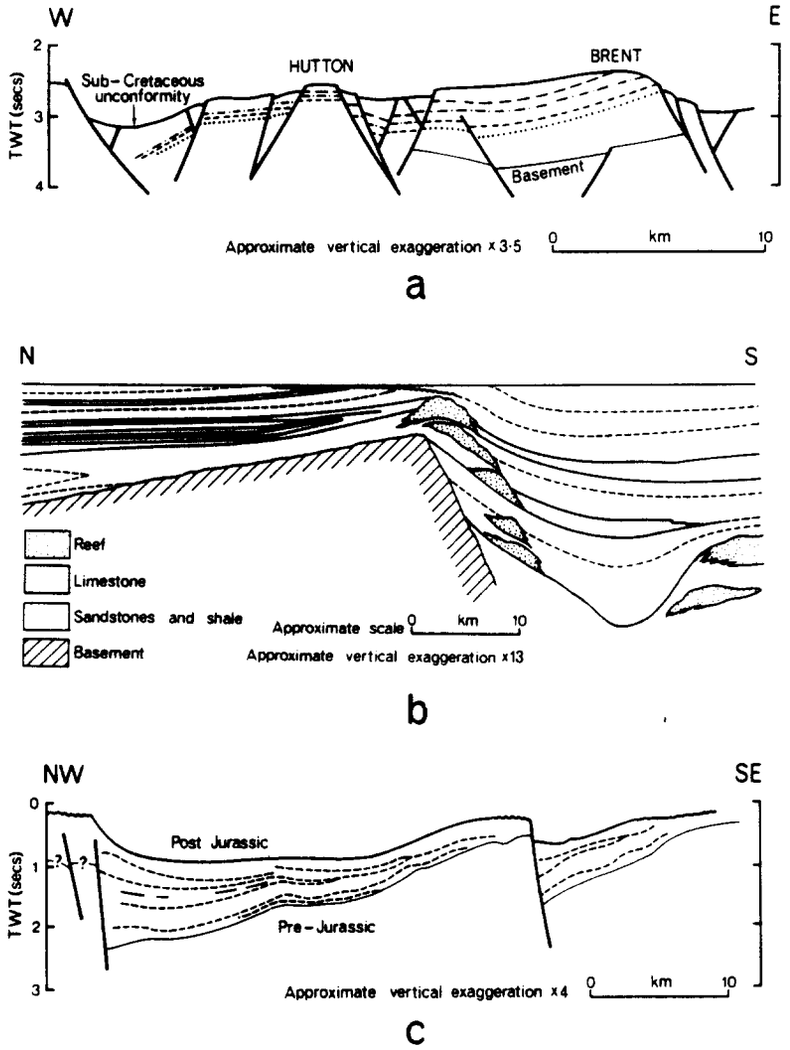

Fig. 11. (a) Cross-section from the North Viking Graben through the Hutton and Brent fields, showing sub-Cretaceous surface and underlying group boundaries. Compare with Fig. 10(b). Note inflection of group boundaries. Redrawn and simplified from Speksnijder (1987, fig. 5). (b) Cross-section of the North Craven fault, northern England, showing primary thinning of footwall sediments towards the footwall cutoff and later erosion on the upper part of the footwall dip slope. Note hangingwall syncline corresponding in position to compactional syncline in Fig. 10(a) and possible onlap of footwall sediments similar to that in Fig. 10(c). Redrawn and simplified from Hudson (1930). (c) Cross-section from the Inner Moray Firth, redrawn and simplified from McQuillan *et al.* (1984, fig. 10/17). Compare with Fig. 10(b) and note primary thinning of sediments towards footwall cutoff, truncations above footwall highs and bedding inflection between faults.

11a) but some footwall erosion has occurred here (Karlsson 1986), and this is not incorporated in the model. Figure 11(b) is a cross-section of the North Craven Fault in northern England, where depositional and erosional thinning of footwall units show that footwall uplift occurred. Hangingwall rollover is present but is modified by a compaction-related hangingwall syncline (Fig. 11b). The bedding inflection and associated lateral variations in stratigraphic thicknesses shown by the model (Fig. 10) are comparable with those associated with actual faults (Figs. 11c and 12a & b, see also Barnett *et al.* 1987).

DISCUSSION

Model dips in the region between two faults (Fig. 10b) are not the products of either tilting or fault block rotation but of the internal deformation which is necessary to accommodate the faults (Barnett *et al.* 1987): a small additional component is due to compaction, which also produces hangingwall compactional synclines. The model does not incorporate the rotations of faults and beds which accommodate regional extension (Barnett *et al.* 1987). Because displacements due to a single fault are local phenomena, as is evident from reverse drag profiles, regional extension or subsidence cannot be obtained by summing displacements on individual faults (Fig. 12b).

Chapman *et al.* (1978), noting that faults within the Kenya Rift typically intersect bedding at right-angles, proposed that the faults initiated as vertical fractures in a horizontal sequence and subsequently rotated to mean dips of 63°. Morton & Black (1975), Angelier & Colletta (1983) and Howard & John (1987) drew similar conclusions from high bedding cutoff angles which may, how-

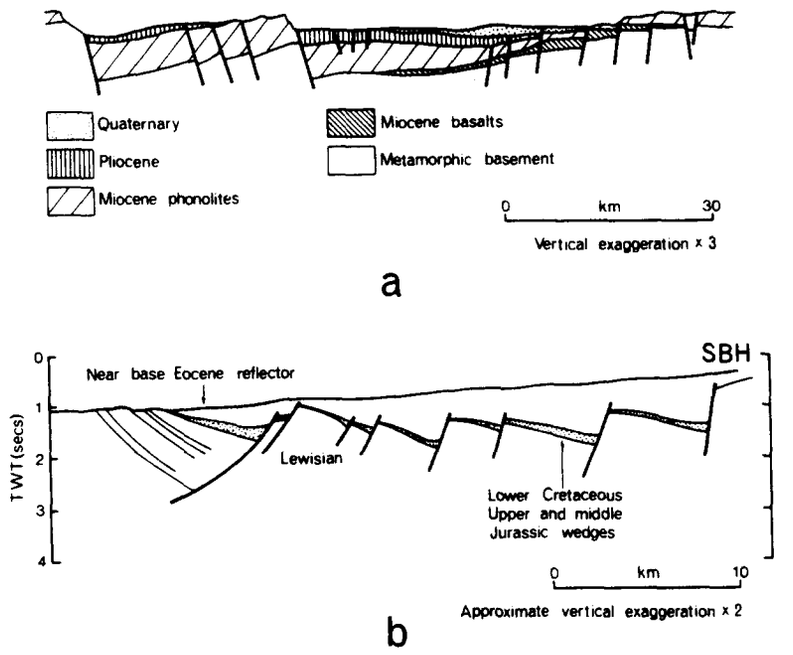

Fig. 12. (a) Cross-section of Kenya Rift Valley at *ca* 0°30'N. The thickness variation of Pliocene volcanics and Miocene phonolites is primary. Displacement on the major fault is distributed approximately 2:1 between hangingwall and footwall. Redrawn from Chapman *et al.* (1978, fig. 9). (b) Cross-section from the continental shelf NW of Orkney showing structure northwestwards from the Solan Bank High (SBH); from Kirton & Hitchen (1987, fig. 7). Note that elevation of Jurassic–Cretaceous wedges is approximately constant, although total down-to-the-west fault throws are equivalent to *ca* 3.5 s two-way travel time (TWT).

ever, be secondary rather than primary phenomena. The angle between bedding and a fault increases as reverse drag develops and, for a 60° dipping fault with displacement of 1 km or greater, originally horizontal bedding will become almost normal to the fault surface (Figs. 6f and 10a). Attempts to restore sections by rotating bedding back to the horizontal can result in anomalously high regional elevations (see Enfield & Coward 1987) and will always give spurious estimates of extension.

Techniques which assume the rollover profile to be a reflection of fault plane geometry (vertical shear or Chevron construction; Verrall 1981) can be applied to hangingwall rollover profiles associated with planar faults; but they will necessarily predict a listric geometry and a depth to detachment estimate which, although meaningless, is consistent with current listric fault extensional models (Beach 1984, 1985, Gibbs 1984a, b, Barr 1985). For example, Chevron analysis of model rollover geometry on a planar fault with displacement of 1–5 km, dip of 45°, and W/D value appropriate to a fault in hard sandstone, yields depth to detachment estimates of 3–6.5 km. For a fault dip of 45–60° the estimated depth to detachment increases to 11 km.

CONCLUSIONS

(1) The displacement field of a single blind normal fault is an ellipsoidal volume with the fault surface as a principal plane.

(2) Variation of displacement in the direction normal to the fault surface, seen as hangingwall rollover and footwall uplift, can be predicted using an empirical expression representing the steady state reverse drag profile attained after many individual slip events on a growing fault.

(3) Expressions for the parameters which determine displacements within a fault volume, i.e. (i) maximum displacement–fault dimension relationship, (ii) fault surface displacement profile and (iii) standard reverse drag profile, can be incorporated in a computer model which generates synthetic structural contour patterns on horizons intersected by a fault.

(4) Synthetic structural contours and cross-sections for an horizon intersected by a fault vary systematically with fault size, fault dip, horizon orientation and position relative to the fault surface. Horizon orientation is particularly important in determining the general pattern of the structural contours.

(5) Footwall uplift and hangingwall subsidence are equal on blind faults. On synsedimentary faults the proportion of displacement accommodated by footwall uplift varies with fault dip and can be predicted.

(6) Synthetic structural contours for synsedimentary faults can be used to represent isopachs of syn-faulting sedimentary units. Primary sedimentary thinning on the footwall and onlap of hangingwall sediments away from the fault are inherent features of the model.

(7) Modelling reproduces many of the essential stratigraphic and structural characteristics of footwall reservoirs. Footwall erosion may obscure primary footwall geometry on seismic sections.

(8) Bed dip between normal faults, which is charac-

teristically opposed to fault dip, is not necessarily a result of fault block rotation but can result from the penetrative deformation which accommodates faulting. An inflection of dip between two faults indicates that the dip is not due solely to block rotation.

(9) A high angle intersection of an horizon with a fault may be a secondary phenomenon, due to penetrative deformation, and does not require the fault to have been originally steeply dipping.

(10) Estimates of depth to a non-existent detachment can be obtained by inappropriate analysis of hangingwall rollover on a planar normal fault.

Acknowledgements—Conrad Childs and Chris Lavers are thanked for their assistance in preparation of the manuscript. Reviewers are thanked for comments which led to significant improvements in presentation. Much of the work was carried out under British Coal contracts YCE.30/19572 and YCE.30/20214 and publication is with the permission of British Coal, but the views expressed are those of the authors and not necessarily those of British Coal.

REFERENCES

Angelier, J. & Colletta, B. 1983. Tension fractures and extensional tectonics. *Nature* **301**, 49–51.

Barnett, J. A. M., Mortimer, J., Rippon, J. H., Walsh, J. J. & Watterson, J. 1987. Displacement geometry in the volume containing a single normal fault. *Bull. Am. Ass. Petrol. Geol.* **71**, 925–937.

Barr, D. 1985. 3-D palinspastic restoration of normal faults in the Inner Moray Firth: implications for extensional basin development. *Earth Planet. Sci. Lett.* **75**, 191–203.

Beach, A. 1984. Structural evolution of the Witch Ground Graben. *J. geol. Soc. Lond.* **141**, 621–628.

Beach, A. 1985. Some comments on sedimentary basin development in the Northern North Sea. *Scott. J. Geol.* **21**, 493–512.

Chapman, G. R., Lippard, S. J. & Martyn, J. E. 1978. The stratigraphy and structure of the Kamasia Range, Kenya Rift Valley. *J. geol. Soc. Lond.* **135**, 265–281.

Chinnery, M. A. & Petrak, J. A. 1968. The dislocation model with a variable discontinuity. *Tectonophysics* **5**, 513–529.

Davison, I. 1986. Listric normal fault profiles: calculation using bed-length balance and fault displacement. *J. Struct. Geol.* **8**, 209–210.

Enfield, M. A. & Coward, M. P. 1987. The structure of the West Orkney Basin, northern Scotland. *J. geol. Soc. Lond.* **144**, 871–884.

Gibbs, A. D. 1983. Balanced cross-section construction from seismic sections in areas of extensional tectonics. *J. Struct. Geol.* **5**, 153–160.

Gibbs, A. D. 1984a. Structural evolution of extensional basin margins. *J. geol. Soc. Lond.* **141**, 609–620.

Gibbs, A. D. 1984b. Clyde Field growth fault secondary detachment above basement faults in North Sea. *Bull. Am. Ass. Petrol. Geol.* **68**, 1029–1039.

Howard, K. A. & John, B. E. 1987. Crustal extension along a rooted system of imbricate low-angle faults: Colorado River extensional corridor, California and Arizona. In: *Continental Extensional Tectonics* (edited by Coward, M. P., Dewey, J. F. & Hancock, P. L.). *Spec. Publs geol. Soc. Lond.* **28**, 299–311.

Hudson, R. G. S. 1930. The Carboniferous of the Craven Reef Belt; the Namurian unconformity at Scalebar, near Settle. *Proc. Yorks. geol. Soc.* **21**, 290–320.

Jackson, J. A. & McKenzie, D. 1983. The geometrical evolution of normal fault systems. *J. Struct. Geol.* **5**, 471–482.

Karlsson, W. 1986. The Snorre, Statfjord and Gullfaks oilfields and the habitat of hydrocarbons on the Tampen Spur, offshore Norway. In: *Habitat of Hydrocarbons on the Norwegian Continental Shelf* (edited by Spencer, A. M.). Graham & Trotman, London, 181–197.

Kasahara, K. 1981. *Earthquake Mechanics*. Cambridge University Press, Cambridge.

Kirton, S. R. & Hitchen, K. 1987. Timing and style of crustal extension N of the Scottish mainland. In: *Continental Extension Tectonics* (edited by Coward, M. P., Dewey, J. F. & Hancock, P. L.). *Spec. Publs geol. Soc. Lond.* **28**, 501–510.

Kusznir, N. J., Marsden, G. & Egan, S. S. 1988. Fault block rotation during continental lithosphere: a flexural cantilever model. *Geophys. J. R. astr. Soc.* **92**, 546.

Masinha, L. & Smylie, D. E. 1971. The displacement fields of inclined faults. *Bull. seism. Soc. Am.* **61**, 1433–1440.

McQuillin, R., Bacon, M. & Barclay, W. 1984. *An Introduction to Seismic Interpretation*. Graham & Trotman, London.

Morton, W. H. & Black, R. 1975. Crustal extension in Afar. In: *The Afar Region of Ethiopia and Related Rift Problems* (edited by Pilger, A. & Rosler, A.). Scheizerbert, Stuttgart, 55–65.

Rippon, J. H. 1985. Contoured patterns of the throw and hade of normal faults in the Coal Measures (Westphalian) north-east Derbyshire. *Proc. Yorks. geol. Soc.* **45**, 147–161.

Savage, J. C. & Hastie, L. M. 1966. Surface deformation associated with dip-slip faulting. *J. geophys. Res.* **71**, 4897–4904.

Scholz, C. H., Aviles, C. A. & Wesnousky, S. G. 1986. Scaling differences between large interplate and intraplate earthquakes. *Bull. seism. Soc. Am.* **76**, 65–70.

Sibson, R. H. 1986. Rupture interaction with fault jogs. In: *Earthquake Source Mechanics* (edited by Das, S., Boatwright, J. & Scholz, C. H.). *Am. Geophys. Un. Monogr.* **37**, *Maurice Ewing Volume* **6**, 157–167.

Speksnijder, A. 1987. The structural configuration of Cormorant Block IV in context of northern Viking Graben structural framework. *Geologie Mijnb.* **65**, 357–379.

Stein, R. S. & Barrientos, S. E. 1985. The 1983 Borah Peak, Idaho, earthquake; geodetic evidence for deep rupture on a planar fault. *U.S. Geol. Survey Open File Rep.* 85–290, 459–484.

Steketee, J. A. 1958a. On Volterra's dislocations in a semi-finite elastic medium. *Can. J. Phys.* **36**, 192–205.

Steketee, J. A. 1958b. Some geophysical applications of the elastic theory of dislocations. *Can. J. Phys.* **36**, 1168–1198.

Verrall, P. 1981. Structural interpretation with applications to North Sea problems. Course notes, Joint Association of Petroleum Exploration Courses (JAPEC), London.

Walsh, J. J. & Watterson, J. 1987. Distribution of cumulative displacement and seismic slip on a single normal fault surface. *J. Struct. Geol.* **9**, 1039–1046.

Walsh, J. J. & Watterson, J. 1988a. Analysis of the relationship between displacements and dimensions of faults. *J. Struct. Geol.* **10**, 239–247.

Walsh, J. J. & Watterson, J. 1988b. Dips of normal faults in British Coal Measures and other sedimentary sequences. *J. geol. Soc. Lond.* **145**, 859–873.

Walsh, J. J. & Watterson, J. 1989. Displacement gradients on fault surfaces. *J. Struct. Geol.* **11**, 307–316.

Watterson, J. 1986. Fault dimensions, displacements and growth. *Pure & Appl. Geophys.* **124**, 365–373.

Wernicke, B. & Burchfiel, B. C. 1982. Modes of extensional tectonics. *J. Struct. Geol.* **4**, 105–115.

Wheeler, J. 1987. Variable-heave models of deformation above listric normal faults: the importance of area conservation. *J. Struct. Geol.* **9**, 1047–1049.

White, N. J., Jackson, J. A. & McKenzie, D. P. 1986. The relationship between the geometry of normal faults and that of the sedimentary layers in their hanging walls. *J. Struct. Geol.* **8**, 897–909.

Williams, G. D. & Vann, I. 1987. The geometry of listric normal faults and deformation in their hangingwalls. *J. Struct. Geol.* **9**, 789–795.